

Research Paper

Residual stress analysis of in situ surface layer heating effects on laser powder bed fusion of 316L stainless steel



William L. Smith ^{a,b,*}, John D. Roehling ^c, Maria Strantza ^c, Rishi K. Ganeriwala ^a, Ava S. Ashby ^a, Bey Vrancken ^c, Bjørn Clausen ^d, Gabriel M. Guss ^a, Donald W. Brown ^d, Joseph T. McKeown ^c, Michael R. Hill ^b, Manyalibo J. Matthews ^c

^a Engineering, Lawrence Livermore National Laboratory, Livermore, CA 94550, USA

^b Mechanical and Aerospace Engineering, University of California Davis, Davis, CA 95616, USA

^c Physical and Life Sciences, Lawrence Livermore National Laboratory, Livermore, CA 94550, USA

^d MST-8, Los Alamos National Laboratory, Los Alamos, NM 87545, USA

ARTICLE INFO

Keywords:

Residual stress
Contour method
Neutron diffraction
Powder bed fusion
Annealing

ABSTRACT

Fabricating parts using laser powder bed fusion (LPBF) is of growing interest to many fields, ranging from medical to aerospace, but this process is often plagued with residual stresses that can reach magnitudes as high as the yield strength of the material. Previous work has demonstrated the ability to reduce residual stress during LPBF by over 90% using an in situ annealing method that makes use of large area, shaped light illumination from a set of laser diodes. In this work, an in-depth analysis of the effectiveness of this in situ residual stress reduction technique is presented. A custom LPBF system was used to fabricate 316L stainless steel parts, and the stresses of these parts were analyzed using the contour method and neutron diffraction on various planes within the samples. These spatial measurements revealed stress reductions near the edges and base of the samples in each of the three measured orthogonal stress directions, in addition to an overall reduction in stress owing to in situ application of laser diode heating. The experimental results were found to be in excellent agreement with numerical thermomechanical simulations that captured the effects of various processing parameters. Furthermore, in cases where the annealing was only performed once every 5 layers, the residual stress was similarly reduced, which indicates that further optimization might be achieved to limit additional processing time during the builds while still relieving equivalent amounts of stress.

1. Introduction

Additive manufacturing (AM) is an ever-growing method of fabricating complex products for commercial use, typically requiring fewer fabrication steps than traditional manufacturing [1]. Due to this high level of interest in metal AM within the industrial space, there is a need to improve upon print consistency when utilizing this process. It is not uncommon for there to be macroscopic part-to-part variability present within additively manufactured parts, which can give rise to print failures and catastrophic defects that greatly reduce part service life or even prevent successful completion of the build altogether [2]. These inconsistencies have motivated the commercialization of layer-by-layer in situ process monitoring within AM, especially for the laser powder bed fusion (LPBF) process [3].

One of the major concerns for parts made using the LPBF process, and

the focus of this work, is the formation of residual stress. Due to the repeated melting and solidification experienced during LPBF, which consists of rapid heating and cooling cycles at rates up to $\approx 10^6$ K/s [4], printed parts are subject to high temperature gradients which can produce large residual stresses [5]. These residual stresses can lead to a wide range of macroscopic defects including warping, cracking, and even delamination from the build plate, which all contribute to lowering the print consistency of LPBF machines [6–9]. Given that post-build annealing would not affect this high potential for print failure, having the ability to reduce residual stresses induced during LPBF in situ is very appealing.

Given that large stresses are typical within welds used to conjoin multiple pieces of material, it follows that LPBF parts will have large residual stresses since the entire part is formed through a process consisting of repeated melting and solidification cycles [10]. The high

* Corresponding author at: Engineering, Lawrence Livermore National Laboratory, Livermore, CA 94550, USA.

E-mail address: smith483@lbl.gov (W.L. Smith).

temperature gradients inherent to LPBF lead to non-uniform thermal expansions which cause localized plastic yielding (deformation) of the metal. As the metal affected by the melting laser is being heated, it expands and softens, lowering its yield strength. The expansion of this softer metal is restricted by the surrounding cooler and stronger (higher yield strength) metal, causing plastic deformation of the soft material, and generating compressive strain. This hot and plastically compressed material begins to contract as it cools, but this contraction is constrained by the still stronger and cooler surrounding material. This constrained contraction converts the stresses within the recently melted material from compressive to tensile, which in turn is balanced out by compressive stresses in the cooler material [10,11].

In an ideal situation, a material could be produced without any residual stresses by ensuring that there were no deformation gradients present at any point during its formation. In practice however, the best way to reduce residual stress formation is to minimize the temperature gradients and rapid cooling rates, which can be difficult to accomplish within LPBF due to the small ($\approx 100 \mu\text{m}$) spot size of the heating source. Since residual stress in any given material cannot exceed its yield strength, heating a part up to an annealing temperature and cooling it slowly and uniformly will reduce the internal stresses to a level below the yield strength of the material (at the annealing temperature) [12]. Logically, many of the simplest and most common methods utilized to reduce residual stress in printed parts involve secondary heating, which include but are not limited to preheating the build plate during printing, heating the entire build chamber, or annealing the parts in a furnace after printing [9,13,14]. Though it was not explored in this work, the scanning strategy can also affect the resulting residual stress based on path length and the scanning speed [6,10,11,15–17]. Temperature gradients within LPBF are generally known to play a major role in the magnitude of residual stresses. However, it has been shown that the distribution of the final residual stress state is highly dependent on the solidification shrinkage mechanism dictated by the scanning pattern [18].

Although residual stress cannot be measured directly, there are several available techniques which measure associated properties (such as cutting-induced deformation or atomic spacing) and determine residual stress through data analysis. Among the techniques for determining residual stress are mechanical methods such as the hole drilling method [19], the slitting method [20,21], the contour method [22,23], and the bridge curvature method (BCM) [24]. There are also diffraction-based methods such as neutron diffraction [25] and X-ray diffraction [26,27], of which the former can allow for characterization of the internal stresses beneath the surface of the sample [9]. Since these residual stress measurement methods rely on very different assumptions and can have systematic errors [28], it is useful to make measurements with complementary techniques (e.g., a mechanical relaxation method and a diffraction method) and then use the full set of results as part of an engineering analysis [25]. Moreover, the contour method provides a single stress component along a given plane with high spatial resolution (0.05–1 mm) in 2D, whereas neutron diffraction provides three stress components for each measurement location (which can be placed at arbitrary locations within the sample) with low spatial resolution in 2D (typically 2 mm). A prior study by the authors [12] used the BCM to compare general levels of residual stress in LPBF samples as a function of in situ annealing temperature, but this method only provides a limited assessment of the full residual stress state (i.e., the bending portion of the stress field).

In the present study, we assess the effect of in situ surface layer heating on the reduction of residual stress in rectangular 316L stainless steel samples printed through the LPBF process. A set of high power (kW) laser diodes was used as the in situ heating source which illuminated the recently scanned and solidified surface layer with homogeneous intensity immediately after the surface layer was complete. It is hypothesized that this surface layer heating/cooling strategy will introduce sufficient annealing into the LPBF process to achieve residual

stress reduction, with the magnitude of stress reduction dependent on the degree of heating and the resulting thermal history. Residual stress is determined in samples subject to differing annealing strategies using two complementary stress measurement techniques, neutron diffraction and the contour method. Thermomechanical modeling is also performed to estimate the residual stress, providing a useful comparison with the experimental results. By utilizing these specific measurement and simulation techniques, we advance the understanding of in situ surface layer annealing beyond that of our prior study using only BCM. Additionally, we assess a variation in annealing strategy, comprised of annealing less frequently, to determine whether residual stress reduction could be accomplished more economically.

2. Methods

2.1. Experimental setup

All samples produced in this study were printed using a small-scale custom LPBF system (Fig. 1A and B) that was developed based on the work presented by Matthews et al. [29]. This system consists of two primary heat sources, the first being an nLight scanning fiber laser (1078 nm, 1 kW) and the second a set of four Trumpf laser diodes (1000 nm, 1.25 kW each). The four laser diodes are focused into a homogenizer that combines the individual laser profiles into a single beam of light that has near homogeneous spatial intensity as it exits the outlet of the homogenizer. This uniform intensity diode beam is passed through an aluminum mask, which clips and shapes the beam projection into an area such that it matches the desired layer pattern at the 25.4 mm diameter build plate surface. The diode light (775 W/mm² maximum) is then reflected from a dichroic mirror onto the build plate. The focused scanning laser with a $1/e^2$ diameter of 80 μm , which is directed by a Nutfield 3XB galvanometer mirror scanner, passes through this same dichroic mirror and is coincident with the diode laser light. The build plate, along with a powder spreader and powder feed system, is housed within a glovebox filled with argon to an O₂ level of <0.01% (100 ppm, Fig. 1C). Custom LabView software is used to control the lasers and powder distribution system.

This study used rectangular specimens built with dimensions of approximately 20 mm (L) \times 10 mm (W) \times 10 mm (H) on build plates 25.4 mm in diameter and 12.7 mm thick (Fig. 1D). Thicker build plates were selected than those used in the authors' previous study (6.35 mm) to prevent potentially catastrophic warping due to an anticipated higher magnitude of residual stress. The scanning laser was held at a constant power and speed of 250 W and 278 mm/s, respectively. These parameters were chosen to maximize part density (above 99%) as well as minimize evaporation from the melt pool due to its proximity to the build window. Layers were scanned using a single contour pass around the perimeter and a crosshatch scan strategy within the interior where the scanning vectors were angled 45° with respect to the longitudinal axis of the part was rotated 90° between each layer.

For samples that were annealed in situ, the diodes illuminated the build area immediately after the focused melting laser finished its scan (Fig. 1C). The diode light was imaged from the mask plane onto the recently scanned and solidified material while the adjacent powder was not illuminated. Applying the diode illumination in this way ensures consistent density and dimensions across samples. The diodes were initially applied at their maximum set power levels, followed by varying power ramps (Table 1). An example of a diode annealing power profile is provided in Fig. 2. The individual power profiles were chosen based on the maximum achievable in situ annealing temperature for a given diode laser power level.

2.2. Thermal measurements

Thermal imaging was used to measure the surface temperature of parts throughout the annealing process. A commercial pyrometer

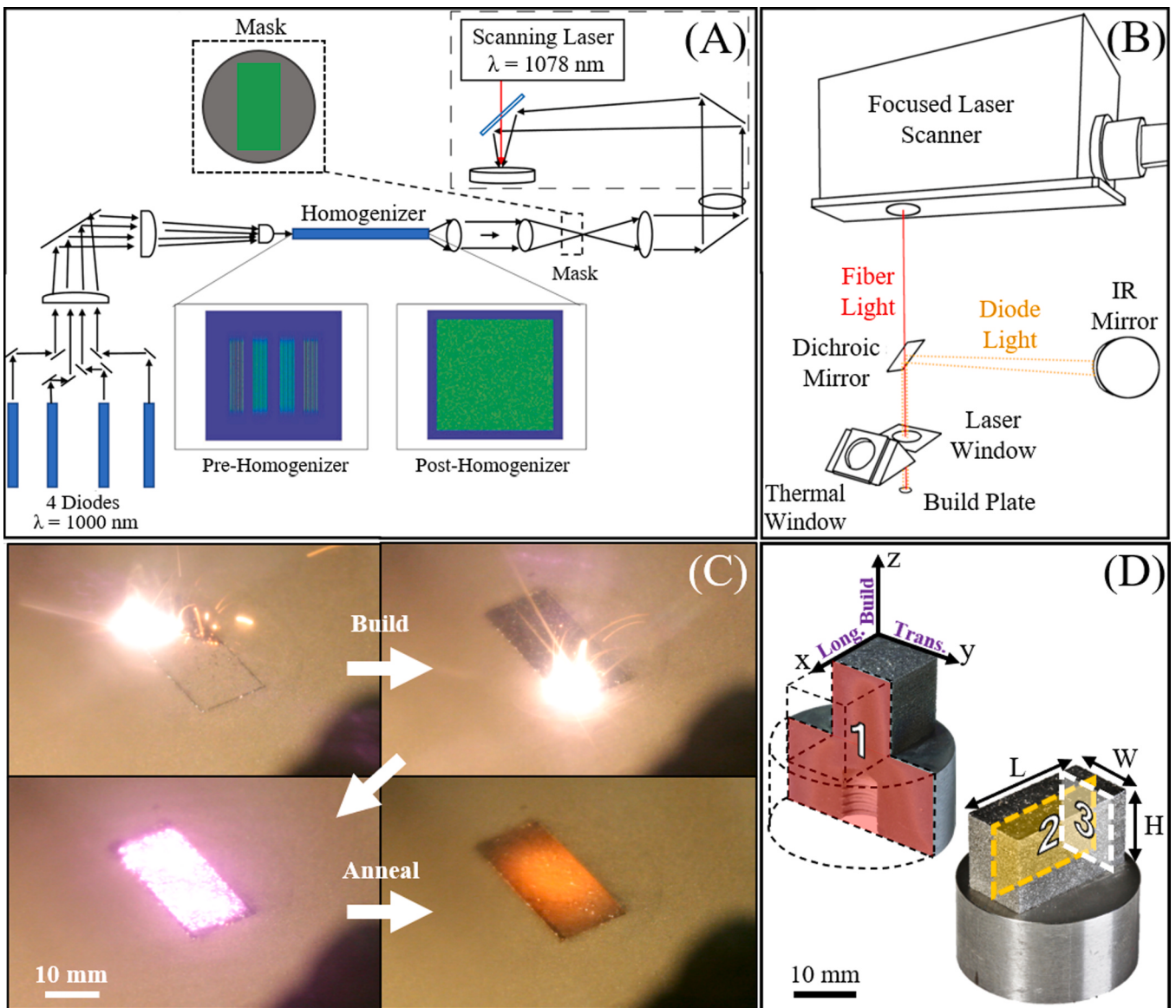


Fig. 1. (A, B) Schematic of the diode annealing LPBF system. (C) Photos of the layer melting and annealing steps within the glovebox build chamber. (D) Photos of printed samples before and after sectioning, labeled with dimensions and stress directions (longitudinal, transverse, and build). Plane 1 represents the contour measurement plane while planes 2 and 3 represent the two neutron diffraction sampling planes within the uncut sample.

Table 1

Processing parameters for the printed samples and their measured annealing temperatures. Stress measurements were made along the edge plane using neutron diffraction for samples listed in bold.

Diode laser power (W)	Maximum diode power density (W/mm^2)	Soak time (s)	Ramp time (s)	Diode energy density (J/mm^2)	Approximate annealing temperature ($^\circ\text{C}$)	Length (mm)	Width (mm)	Height (mm)
0	0	0	0	0	N/A	20.12	10.30	11.23
2600	4.42	0	5	11.05	700	22.46	10.20	11.31
2600	4.42	2	5	19.90	1000	19.84	10.23	10.40
3000	5.10	10	0	51.01	950 (every 5 layers)	19.86	10.15	12.08

(Omega IR2C) was used to measure the surface temperature of samples throughout the annealing process and was positioned to be orthogonal to the 3 mm thick anti-reflective BK7 optical viewing window (Fig. 1B), approximately 50 cm from the build surface. This pyrometer used wavelengths between 400 and 1600 nm to measure an average temperature over a circular area of approximately 10 mm in diameter at the center of the top layer. An optical notch filter was placed over the pyrometer probe to filter out the diode light. The pyrometer was capable of

two-color pyrometry, but due to the required optical filter (to filter the diode light), anomalous temperatures resulted when using two-color mode. Therefore, the one-color mode was used after calibrating the emissivity.

Emissivity calibrations were performed by spot welding a thermocouple to the bottom of a 25.4 mm diameter 316L stainless steel disk of 500 μm thickness and insulating the bottom of the disk with 25.4 mm thick alumina wool. A thin disk was used to minimize the temperature

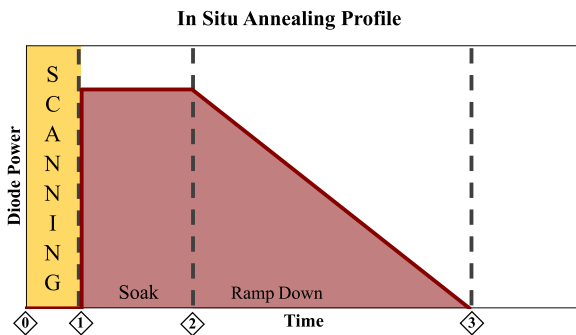


Fig. 2. An example of a diode annealing power profile. (0) The fiber laser is scanning and melting the loose powder (1) Melting ends and laser diode emission initiates at full power and maintains for the duration of the soak (2) Soaking ends and the diodes ramp down from maximum power to 0 W (3) Annealing is complete.

drop between the top surface to the thermocouple on the underside. The diodes were then turned on to provide a heat source to the top side of the disk. The emissivity (0.45) was adjusted until the pyrometer and thermocouple readings were within 20 ± 2 °C throughout the entire measurement range (300–1300 °C). This calibration method was required because the diode light was within the measurement band of the pyrometer. Both the presence of the optical filter and the operation of the diodes caused slight changes in the apparent temperature readings, which were minimized by using this calibration method. Calibration performed using a ceramic heater to heat the stainless steel disk and measuring the temperature on the top side with both the thermocouple and IR pyrometer did not yield accurate results when using the diodes to heat the surface.

2.3. Residual stress characterization

Two independent stress characterization approaches were carried out in this study, specifically the contour method and neutron diffraction. In the contour method [28], samples are sectioned using wire electrical discharge machining (EDM), which relieves internal stresses along this cut plane and creates two mirror-imaged surfaces. The height profiles of the two cut surfaces are measured to determine the displacements that resulted from the stress relieved by the cut, which can be performed using a coordinate measuring machine or a non-contact optical scanner [30]. The profiles of the two cut surfaces are aligned, overlapped, averaged, and smoothed to remove noise. This processed profile data is first inverted about the surface normal and is then used as a displacement boundary condition applied to the cut surface of a 3-dimensional representation of the sample within finite element method software. The resulting stresses normal to the cut surface represent the residual stresses present prior to sectioning [28,30]. Without being removed from their build plates, the as-printed samples were securely clamped and sectioned down the middle, orthogonal to the long axis of the samples at plane 1 (Fig. 1D). All cutting was performed using a 152 µm (0.006 in.) diameter brass wire at 726 µm/min (0.03 in./min). A Keyence VR microscope profile scanner was used to optically measure height contour data on a grid of points with approximately 60 µm spacing in each direction. The contour data was processed in MATLAB and smoothed using a 3rd-order surface spline fit, which was then applied to a 3D representation in an elastic COMSOL Multiphysics® finite element model. More information on typical implementation of the contour method can be found in References [28, 30].

Neutron diffraction is a technique that can non-destructively measure the lattice parameters of the stressed samples beneath the surface. The neutron diffraction measurements were performed on the SMARTS instrument (Spectrometer for Materials Research at Temperature and

Stress) at Los Alamos Neutron Science Center (LANSCE) [31]. The LANSCE accelerator produces a pulsed (20 Hz) incident neutron beam that results in a wavelength spectrum from 0.5 to 7.5 Å on the SMARTS instrument. During the measurements, the incident beam was masked by boron nitride slits to a cross section of 2×2 mm². Two detector banks employing 3He tubes positioned at +90° and -90° from the incident beam were used to measure the diffracted neutrons using the time-of-flight (TOF) technique. The through thickness resolution was defined by a set of radial collimators with an acceptance length of 2 mm that were located in front of the detectors, and as a result, the presented diffraction measurements have a sampling volume of $2 \times 2 \times 2$ mm³. To measure the three orthogonal strain components (ϵ_{ii}), each sample was measured in two orientations with respect to the detectors, first horizontally and then vertically. The as-built averaged lattice strains were determined in the three orthogonal directions at points that were at least 1.75 mm away from the nearest surface to ensure that the sampling volume was always fully embedded within the sample.

The collected diffraction patterns were used to determine the lattice parameters through Rietveld refinement of the full diffraction pattern using the GSAS software [32] and the SMARTSware refinement routines [33]. The determined lattice parameters were then used to calculate the three orthogonal strain components: longitudinal (ϵ_{ii}), transverse (ϵ_{jj}), & build (ϵ_{kk}) from:

$$\epsilon_{ii} = \frac{a_{ii} - a_{0,ii}}{a_{0,ii}}, \quad (1)$$

where a_{ii} is the averaged lattice parameter of the measured sample along direction ii and $a_{0,ii}$ is the stress-free averaged lattice parameter. The stress-free lattice parameter was measured on a $3.7 \times 3.5 \times 3.3$ mm³ rectangular prism that was extracted from the center of a non-annealed sample via wire EDM. The reference sample was extracted with differing sides to facilitate keeping track of its orientation within the printed part (i.e., longitudinal, transverse, and build directions). Though a portion of the stress gradients that were originally present in the region from which the reference sample was extracted may remain in the reference sample, extracting a rectangular prism of this size using wire EDM significantly relieves its internal stresses while ensuring the sampling volume of the beam fits comfortably within the prism [34]. The lattice parameters of this assumed stress-free sample served as a reference to which the lattice parameters of all other printed samples would be compared to calculate their strains.

As discussed by Daymond [35], using the lattice parameter determined from Rietveld refinement ensures that the determined lattice strain is representative of the bulk average strain in the gauge volume, and thus the normal continuum mechanics material parameters (Young's modulus and Poisson's ratio) can be used when calculating the residual stresses from the measured strains. The strains (ϵ_{ii}) are used to compute stresses (σ_{ii}) based on the material properties of the samples using Hooke's law:

$$\sigma_{ii} = \frac{E}{(1+\nu)(1-2\nu)} \left((1-\nu)\epsilon_{ii} + \nu(\epsilon_{jj} + \epsilon_{kk}) \right), \quad (2)$$

where ii , jj , & kk represent each of the three orthogonal stress and strain components, E is the Young's modulus (200 GPa), and ν is the Poisson's ratio (0.3) of 316L stainless steel [36,37]. For each sample, a total of 45 evenly-spaced measurements were made across the central longitudinal plane ($y = W/2$) of the as-printed sample in a 9×5 array, as indicated by Plane 2 in Fig. 1D. Additionally, two samples (see Table 1) were measured along the transverse plane 1.75 mm from the edge of the part in a 5×5 data point array, as indicated by plane 3 in Fig. 1D.

2.4. Numerical simulations

The multi-physics finite element code, Diablo [38], developed at Lawrence Livermore National Laboratory, was used to perform

thermomechanical simulations of the build process and forecast residual stresses for the given range of build and annealing conditions. Diablo is an implicit, Lagrangian code with distributed memory parallelism. The balance of energy is solved throughout the domain Ω :

$$\rho c_p \dot{T} = \nabla \cdot (k \nabla T) + \psi_{ext}, \text{ in } \Omega, \quad (3)$$

where ρ is the density, c_p is the constant pressure specific heat, T is temperature, k is the isotropic thermal conductivity, and ψ_{ext} represents the volumetric heat input from external sources such as the melting laser and the diodes.

Boundary conditions are prescribed over the surfaces Γ_D , Γ_{Ntop} , and Γ_{Nbot} which represent the portion of the surface with prescribed Dirichlet and Neumann boundary conditions, respectively. They are expressed as follows:

$$\begin{aligned} T(\mathbf{x}, t) &= T_0, \text{ on } \mathbf{x} \in \Gamma_D, \\ q(\mathbf{x}, t) &= \mathbf{q} \cdot \mathbf{n} = h_{bot}(T - T_\infty), \text{ on } \mathbf{x} \in \Gamma_{Nbot}, \\ q(\mathbf{x}, t) &= \mathbf{q} \cdot \mathbf{n} = h_{top}(T - T_\infty) + \sigma_{SB}\varepsilon(T^4 - T_\infty^4), \text{ on } \mathbf{x} \in \Gamma_{Ntop}. \end{aligned} \quad (4)$$

Here, Γ_D is the location where the build plate is bolted to the motion stage that controls movement in the build direction and $T_0 = 303$ K. Γ_{Nbot} is defined as the remainder of the bottom surface of the build plate. As this portion is not directly attached to the substrate via the connecting bolt, a Neumann boundary condition with high convection coefficient of $h_{bot} = 1000$ W/(m² K) and $T_\infty = 303$ K was used to mimic heat transfer to the larger underlying substrate. On the top surface of the sample being built (Γ_{Ntop}), convection and radiation to the external environment are modeled with emissivity, $\varepsilon = 0.3$ and $h_{top} = 40$ W/(m² K) [37]. A depiction of the boundary conditions and mesh used for the part and build plate are shown in Fig. 3A.

The mechanical system is governed by the balance of linear momentum given by,

$$\rho \ddot{\mathbf{x}} = \nabla \cdot \boldsymbol{\sigma} + \mathbf{f}_b, \text{ in } \Omega, \quad (5)$$

where ρ represents density, $\ddot{\mathbf{x}}$ is acceleration, $\boldsymbol{\sigma}$ is the Cauchy stress, and \mathbf{f}_b represents body forces (neglecting gravity, $\mathbf{f}_b = 0$). A zero displacement Dirichlet boundary condition is applied to where the build plate is affixed to the motion stage,

$$\mathbf{u}(\mathbf{x}, t) = 0, \text{ on } \mathbf{x} \in \Gamma_D. \quad (6)$$

The stress is calculated via a strain rate independent plasticity model

with linear isotropic hardening, as described in Hodge et al. [37]. Thermophysical and mechanical properties for 316L SS are also provided in Ref. [37].

In order to perform simulations at the physical layer size, h-type adaptive mesh refinement (AMR) is used [39]. The refinement is programmed to occur in a layer-wise manner, where all refinement/de-refinement occurs at the activation of each new layer. Three levels of isotropic pre-refinement were performed on the part, which is initially meshed with $0.4 \times 0.4 \times 0.4$ mm³ elements. As the element size is halved in each direction during each refinement step, the resulting element size is $0.05 \times 0.05 \times 0.05$ mm³. This allows for activation of 50 μm layers, as is true for the physical process. As each new layer is added, elements at a prescribed number of layers below the top surface are de-refined to minimize the total degrees of freedom in the problem, as illustrated in Fig. 3B. Further details regarding the AMR algorithm are provided in Ref. [40].

Despite using AMR to improve efficiency, simulating each individual laser melting pass remains too computationally expensive to be practical. Thus, the simulations are sped up by applying heat uniformly over an entire layer at once, a technique previously shown capable of producing relatively accurate residual stress predictions [16,41]. The amount of heat applied is calculated such that the total amount of energy deposited is equal to that supplied in the physical process. The volumetric power input during the laser melting portion is given as,

$$\psi_{ext,laser} = \frac{P_a}{Ad} = \frac{1}{t_{flash}} * \frac{\alpha_{melt} P_p}{hvd}. \quad (7)$$

In this equation, P_a refers to the layer agglomerated power, P_p refers to the physical process value, h is hatch spacing, v is scan speed, d is layer thickness, and A refers to the cross-sectional area of the part (200 mm²). The duration of power application (t_{flash}) is set to 0.1 s, which is long enough to allow for complete melting of the new layer. The effective absorptivity value during keyhole melting (α_{melt}) is equal to 0.7, which was determined via experimental measurements in Trapp et al. [42].

To model the diode heating phase, energy is again input over the entire top layer,

$$\psi_{ext,diode} = \frac{\alpha_{diode} P_{diode}(t)}{Ad}. \quad (8)$$

where $P_{diode}(t)$ is the applied diode power as a function of time. The absorptivity during diode heating (α_{diode}) is set to 0.3, which is close to

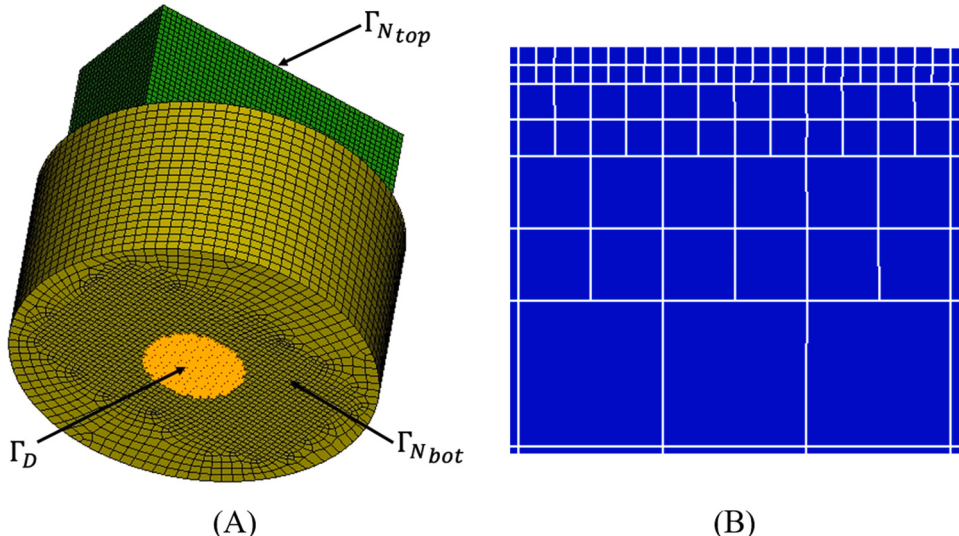


Fig. 3. (A) Depiction of the boundary conditions and initial mesh for the build plate (yellow) and printed block (green). (B) Two-dimensional illustration of the mesh showing three levels of refinement, ranging from 50 to 400 μm in edge length. (For interpretation of the references to colour in this figure legend, the reader is referred to the web version of this article.).

the bare plate absorptivity value for 316L SS since the material has already solidified by this point. Similarly, other process parameters such as the inter-layer time were kept equal to that of the physical process.

3. Results

Contour measurements were performed for each sample listed in Table 1, where samples were sectioned along the central transverse axis using wire EDM (plane 1 in Fig. 1D), providing a map of the longitudinal stress in this central plane ($x = L/2$). Though an uncertainty analysis was not performed in this study, Olson et al. [43] carried out a validation study of a previously developed contour method single-measurement uncertainty estimator [44] and found that modeling error was the largest contributor to the total uncertainty in their measurements while displacement measurement errors had a negligible contribution. This uncertainty was found to be related to elastic modulus, which for the case of 316L stainless steel is approximately 25 MPa ($125 \times 10^{-6} E$) for interior locations and 50 MPa ($250 \times 10^{-6} E$) for locations within 1 mm of the sample boundary. The contour plots in Fig. 4 display the longitudinal stresses normal to the cut surface of each printed sample, with

the horizontal and vertical locations of the stresses normalized to the width and height of each sample (Table 1). Positive (red) and negative (blue) values represent tensile and compressive stresses, respectively. When looking at these longitudinal stresses over the entire cut printed surfaces, reduction in residual stress from in situ annealing is apparent. There is a clear stress magnitude reduction with increased annealing temperature towards the bottom of the samples, at the interface between the printed sample and the build plate. As expected, the stresses are symmetric about the central vertical axis of the printed samples. Based on these contour measurements, comparable stress reduction is achieved when annealing less frequently (950 °C/5 layers) as opposed to annealing every layer (1000 °C). There is a reduction in overall compressive stress towards the bottom of the samples near the build plate, though the peak stresses closest to the corners remain relatively unchanged. However, there is not a significant reduction in stress near the edge of the annealed samples ($y = 0$ or W). Data near the side edges still show compressive stresses ranging from -100 MPa near the top of the annealed samples to -600 MPa near the corners at the base of the samples. When comparing results from the No Anneal and 700 °C samples in this plane, there is not a significant reduction in stress near

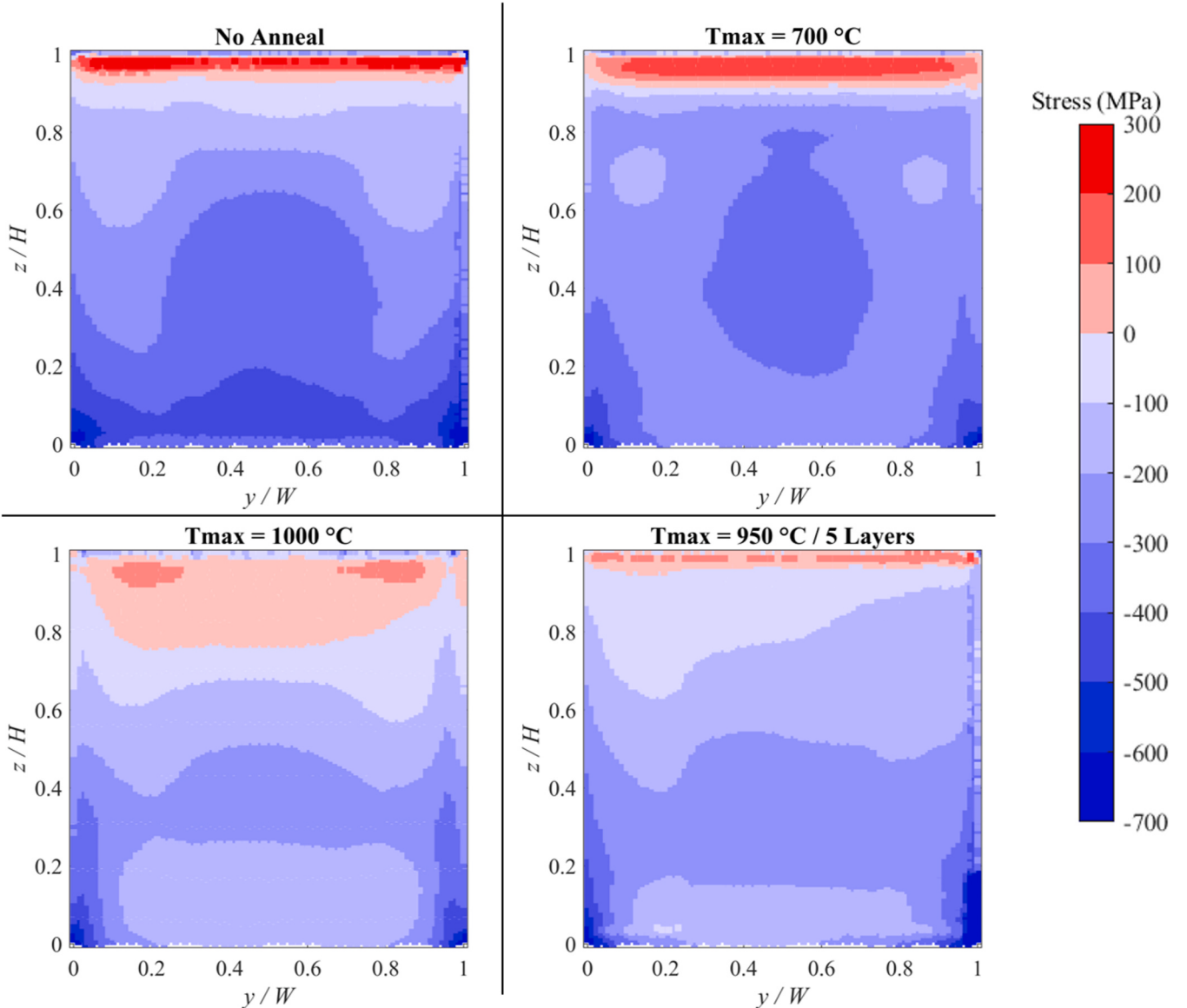


Fig. 4. The longitudinal stress of printed parts as measured using the contour method. Measurements were taken along the cut surface at $x = L/2$ (Plane 1 in Fig. 1D). (For interpretation of the references to colour in this figure legend, the reader is referred to the web version of this article.).

the upper edge ($z = H$), while there is such a reduction at the lower edge ($z = 0$).

Neutron diffraction measurements were made along the central longitudinal plane located at $y = W/2$ for each sample (Plane 2 in Fig. 1D). These neutron diffraction measurements were subject to some experimental uncertainty, which partially derives from the statistical standard deviation of the Rietveld refinement analyses. The resulting stress uncertainties, which propagate from the strain uncertainties, are approximately ± 14.6 MPa on average with a maximum uncertainty of ± 35.9 MPa. Similar to the contour measurements shown in Fig. 4, the surface plots shown in Fig. 5 display an overall reduction in longitudinal stress throughout the neutron diffraction measurement plane with increased annealing temperature. There is a reduction in compressive stress in the longitudinal direction at the center of the printed samples as annealing temperature is increased. There is also a reduction in compressive stresses near the bottom of the samples, but data is not available close to the sample boundaries (closer than 1.75 mm from all edges) due to the constraints of neutron diffraction. Overall, there is a noticeable reduction in the magnitude of the residual stresses over the entire central longitudinal plane. Once again, the stress state of the sample annealed every 5 layers at 950°C is very similar to the sample annealed every layer at 1000°C .

Fig. 6 compares the contour and neutron diffraction measurement data to simulation results. Stresses are compared along the central vertical axis of the printed block. This axis was chosen due to it being at the intersection of the central transverse and longitudinal planes ($x = L/2$, $y = W/2$), along which the contour and neutron diffraction data are sampled, respectively. There is generally good agreement between experimental data obtained using neutron diffraction, contour method, and model predictions. Data obtained from neutron diffraction and the contour method are closely matched while the modeling data deviates slightly for higher temperature samples, showing larger stress magnitudes at the top and bottom of the samples. When comparing the measurements near the top of the sample (1.75 mm from the top surface, or $z = 0.825H$) neutron diffraction data shows the stresses are unaffected by the annealing, with each sample displaying tensile stresses of

approximately 200 MPa. The most noticeable reduction in stress occurs at the bottom of the sample, closer to the build plate. When comparing the samples built with the greatest difference in annealing conditions (No Anneal and 1000°C), the stress for the sample annealed to 1000°C was -24 MPa for the contour measurement closest to the build plate ($z = 0$) while the sample built without any annealing had a -285 MPa compressive stress at this same location, which indicates a stress magnitude reduction of over 90%.

In addition to the measurements of the longitudinal stress, neutron diffraction was also used to measure residual stresses in the transverse and build directions. A comparison of the three orthogonal stress components is plotted in Fig. 7, with all data points taken along the central axis shown in Fig. 7D. There is an observable decrease in stress magnitude with increased annealing temperature, with the most significant reduction present in samples annealed above 700°C . This trend is predicted in the simulation results, which have a strong agreement with the results of the neutron diffraction measurements. The correlation between stress reduction and annealing temperature is particularly evident at the center of the samples ($x = L/2$) for the longitudinal and build stress components, with contour measurement results plotted for comparison in this same location (Fig. 7A). When comparing the sample built without in situ annealing (No Anneal) to the sample that was subject to the highest annealing temperature (1000°C), there is a stress change from compressive towards zero by 160 ± 21 MPa in the build direction and 183 ± 18 MPa in the longitudinal direction. The measured stress state of the sample annealed every 5 layers ($950^{\circ}\text{C}/5$ layers) is very similar to that of the sample annealed every layer (1000°C) in all three directions. Even though the simulations predict a relatively small reduction in transverse stress with increased annealing temperature, this trend is less clear in the corresponding neutron diffraction results (Fig. 7B).

Neutron diffraction measurements were also performed near the short edge ($x = 1.75$ mm) of two of the specimens and the resulting build stresses are plotted in Fig. 8. As predicted by the simulation, stresses in the build direction are tensile at the bottom of the sample, with a region of compressive stresses near the top of each of the samples.

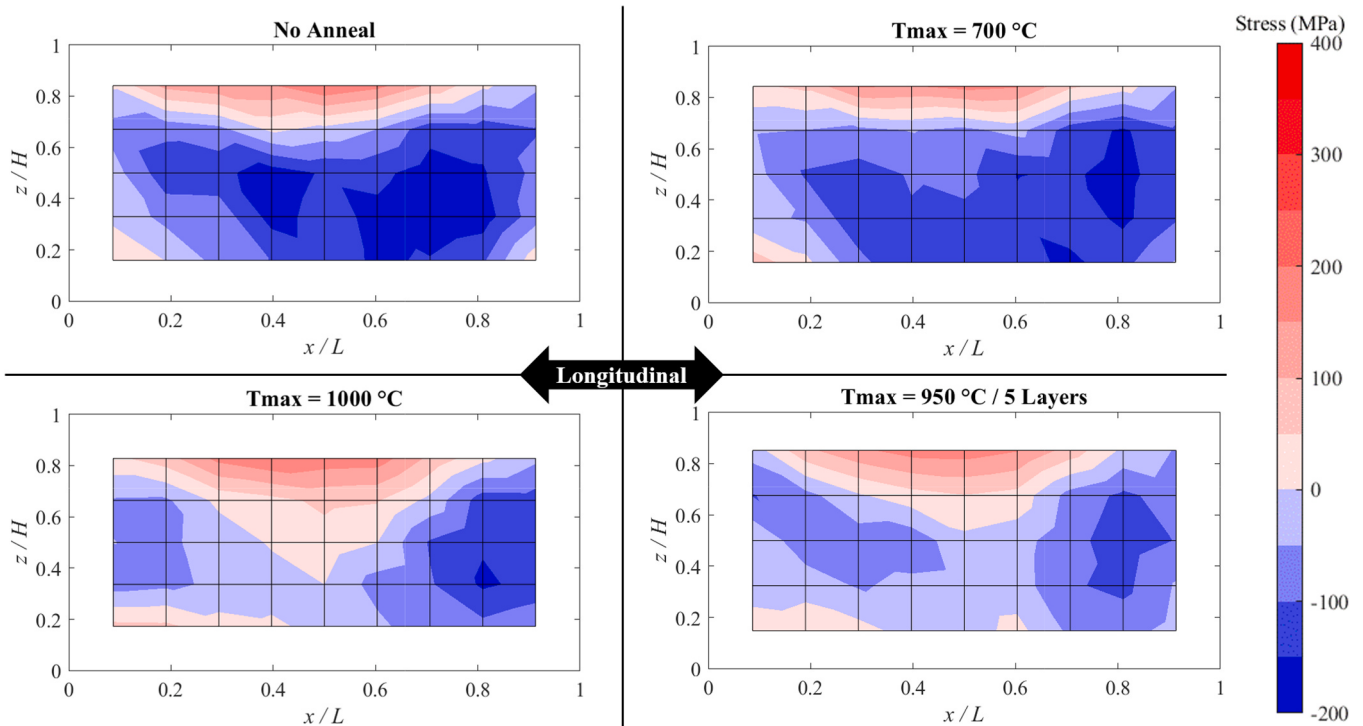


Fig. 5. Longitudinal stress of samples measured using neutron diffraction at $y = W/2$ (Plane 2 in Fig. 1D).

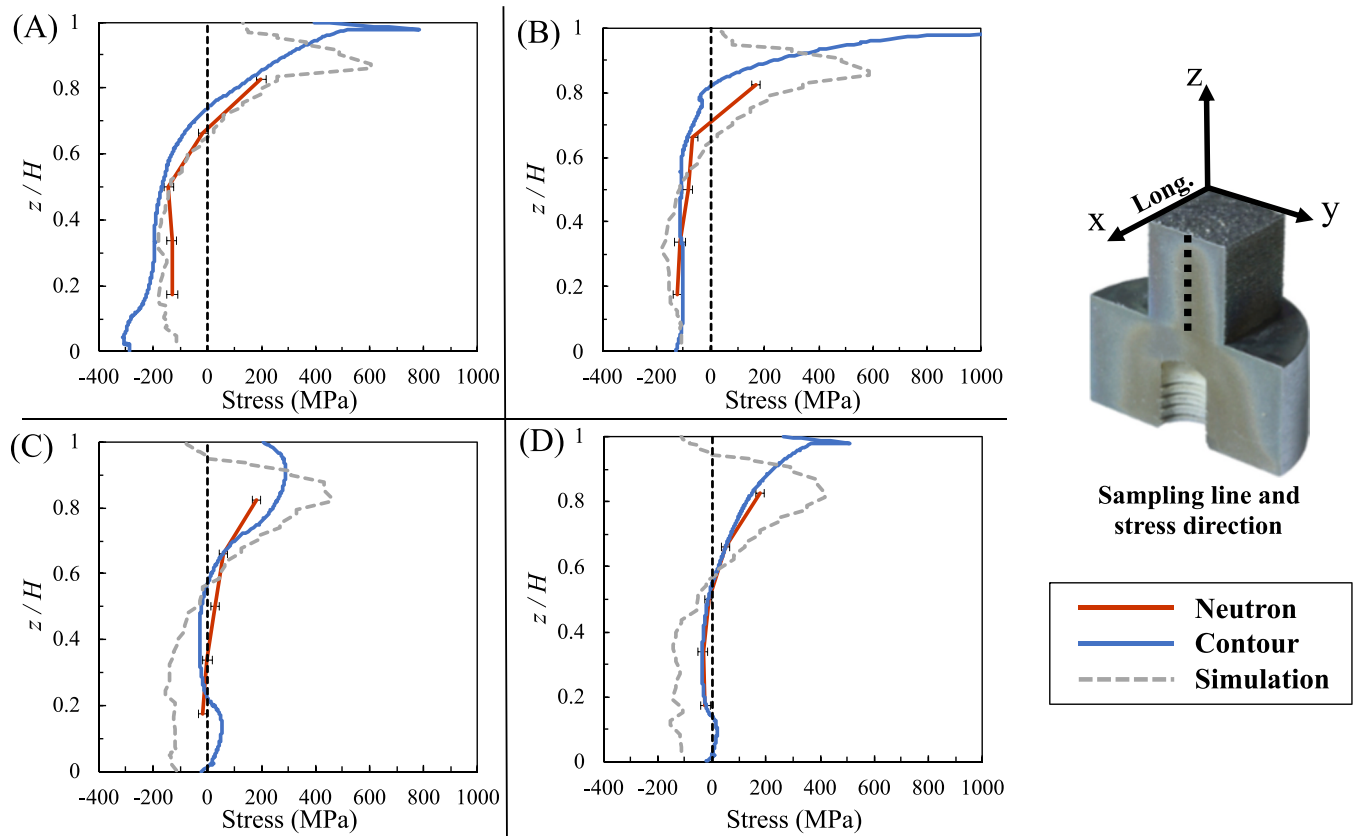


Fig. 6. A comparison of longitudinal stress as determined by neutron diffraction, the contour method, and simulations. Data points are taken from a straight line in the z direction at the center of the samples ($x = L/2$, $y = W/2$). (A) No Anneal, (B) 700 °C, (C) 1000 °C, & (D) 950 °C/5 Layers.

For the sample annealed to 1000 °C, the compressive zone at the top of the sample grows in both size and in stress magnitude, while the tensile stresses in the bottom corners decreased in magnitude from 411 ± 15 MPa of tensile stress to 170 ± 13 MPa after annealing. This stress distribution for the 1000 °C annealed sample differs from its simulated counterpart, which displays an overall reduction in stress magnitudes, but the size of the respective stress zones remains relatively unchanged.

4. Discussion

The final residual stress state of printed parts can be influenced by several factors within the LPBF process including laser scan speed, laser power, and scan strategies, each of which drives the thermal gradients that cause stress. Additionally, complex or multi-component builds are also affected by the “jump” choices made when applying the scanning across the entire layer of a build. In this study, we used direct surface heating between build layers to both reduce stress in the prior layers and to provide a preheat that reduces the temperature gradient in subsequent layers. By keeping all other build parameters constant, we maintain consistent densities, minimize the influence of the solidification rate on our results, and focus solely on the influence of our annealing strategies on the residual stresses.

There is a clear reduction in longitudinal and build stresses when annealing above a critical temperature, as seen in Fig. 7, which correlates to a previously observed decrease in yield stress of austenitic stainless steels above 650 °C [45]. The temperature dependence of the mechanical properties becomes visible when comparing the experimental and simulated results in Fig. 6, particularly when contrasting the lower temperature samples to those annealed to higher temperatures. The model appears to overestimate the stresses above 700 °C, which

may be due increased uncertainty in material properties at higher temperatures [45–47]. There were no significant reductions in stress for the samples annealed below this temperature.

When reducing the frequency of layer annealing, there is still a similar stress reduction when compared to samples annealed every layer within that same temperature range. In the case of the print parameters for the sample shown in Fig. 6D, this means there was sufficient stress reduction even though the total annealing time was roughly 71% shorter than that of a sample annealed every layer. Through our simulation for the sample heated to 950 °C every 5 layers, at a height of $z = 0.7H$ we saw that the maximum temperature at the surface was 985 °C and the temperature 500 μm below it was 936 °C. Given that the heat penetrated sufficiently for the temperature 10 layers below the surface to be within 50 °C of the maximum surface temperature, it seems that sufficient annealing can be accomplished when heating in intervals of at least 10 layers (500 μm), double that tested in this study.

The effect of the penetration depth of the surface annealing can also be seen when comparing stress reductions near the base of the samples versus the top. In Fig. 6, there is less residual stress reduction near the top surface of the sample ($z > 0.7H$) than the lower portion of the sample with increasing annealing temperature. The contour measurements at the very base of the samples ($y = 0$) decrease with each increase in annealing temperature, from -285.9 MPa for the No Anneal sample to -24.2 MPa for the 1000 °C sample, a reduction of over 90%. Meanwhile, those same samples experience only a 47.6% reduction in stress near the top ($y = H$), decreasing from 396.2 MPa for the No Anneal Sample to 207.5 MPa for the 1000 °C sample. This can be attributed to the fact that the lower layers of the samples are subject to a higher number of annealing cycles than the layers closer to the top of the sample due to the penetration depth of the surface layer annealing. It is likely that the tensile stress at the top of the in situ annealed samples

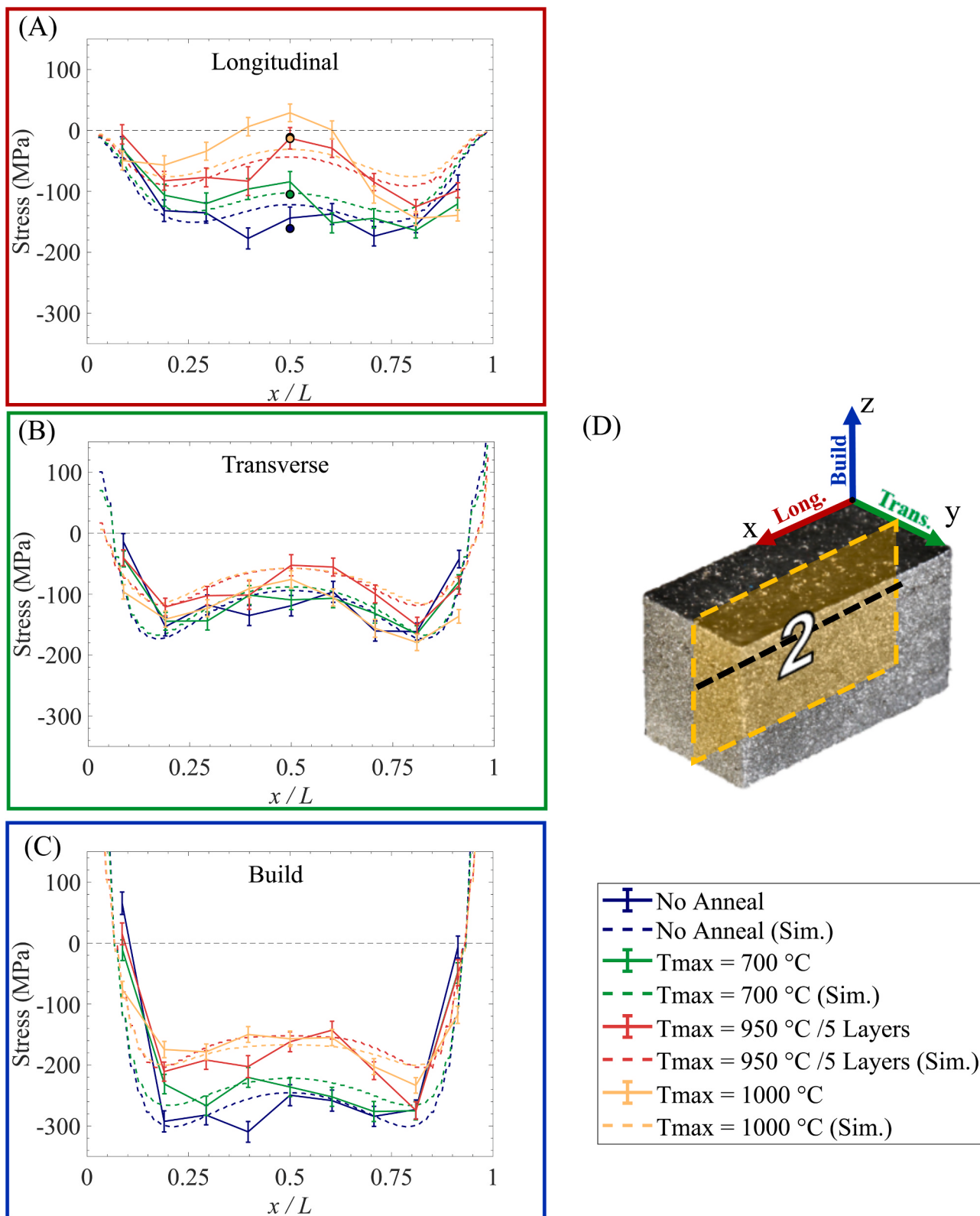


Fig. 7. (A–C) Plots of the stresses measured through neutron diffraction as compared to simulations in each orthogonal stress direction. (A) Longitudinal stress at $x = L/2$ is compared to contour measurements in that same location, as indicated by the bold circles. (D) Each data point is sampled along the length of the printed sample at $z = H/2$ within the neutron sampling plane ($y = W/2$).

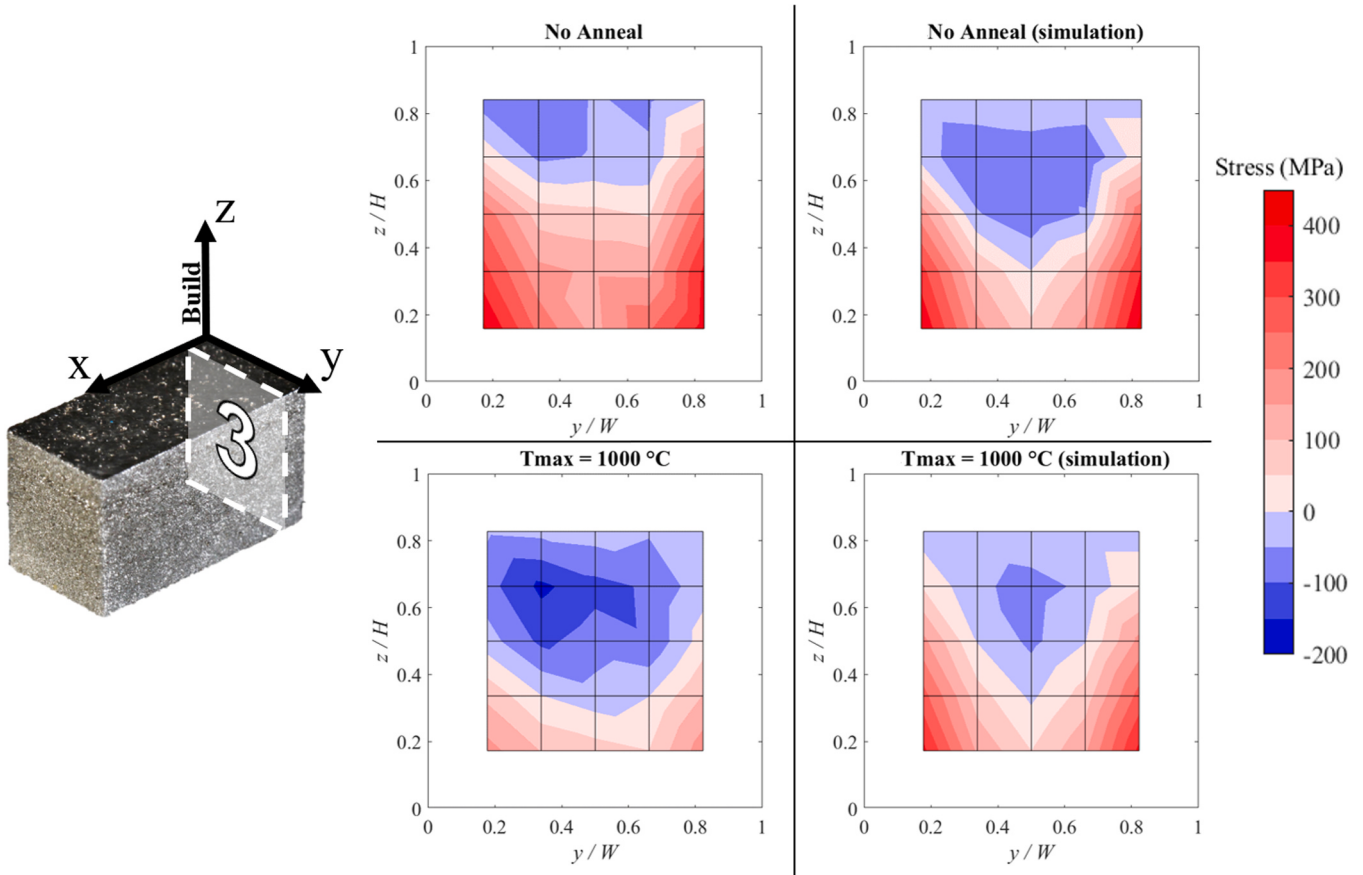


Fig. 8. Build direction stresses data obtained through neutron diffraction experiments and the numerical model at $x = 1.75$ (Plane 3 in Fig. 1D).

(Fig. 4) remain intact because the material in this upper region of the sample spends less time at maximum annealing temperature than the material below it. These observations are similar to the extent of martensite decomposition observed in LPBF of Ti-6Al-4V [48,49], where repeated thermal cycles provided sufficient time and energy for the martensite in lower layers to decompose, whereas the martensite remained present in the top layers.

In the quest to achieve stress-free parts without the need for post-processing, a strategy to completely remove these stresses will need to be developed. To make up for the top layers spending less time at maximum annealing temperatures, a final prolonged soak (in addition to the standard *in situ* annealing) could be performed to further relieve the stresses at the top of the part. To further reduce the stresses within the rest of the part, a reduced thermal gradient during the *in situ* annealing process is needed. Because of the uniform illumination intensity on the top surface of the sample, some degree of lateral temperature gradients are present during annealing. Furthermore, temperature gradients into the thickness of the part are unavoidable due to the heat flux from the surface. Further strategies will need to be developed to tailor the annealing profile to achieve the lowest thermal gradients possible throughout the parts and reduce stresses to the lowest degree possible in as-built parts.

While the stress reduction trend apparent in experimental results correlates well with simulation results, there is not consistent agreement in stress magnitude and spatial distribution. An example of such a disagreement can be observed in the case of the neutron diffraction measurements made on the $x = 1.75$ mm plane (Fig. 8), where there is a difference in build stress for the $1000\text{ }^{\circ}\text{C}$ sample. The compressive zone in the top of the sample is both larger in size and in magnitude for the experimental results than the simulation results. This may be due in part to the nature of the diode projection onto the surface layer of the sample

and the fact that it may not be totally uniform, particularly near the edges. There is a taper in intensity near the edges of the diode projection due to slight beam clipping from the mask and the overall sharpness of the projection. We also made the diode projection area slightly smaller than the area of the top surface to ensure that none of the loose powder adjacent to the build area was subject to the surface annealing, as this could lead to unwanted melting or sintering of the powder and cause issues with spreading on subsequent layers. Since the numerical model simulated heat application to the entire surface, these non-ideal diode projection conditions could be the cause for the discrepancy between the experimental and simulated results close to this edge of the sample.

Though the samples were annealed with consistent laser power throughout the build, surface layer monitoring revealed that the maximum annealing temperature for each layer was not always the same. In the case of the $700\text{ }^{\circ}\text{C}$ sample shown in Fig. 9, the maximum temperature at a height of 1.65 mm was $656\text{ }^{\circ}\text{C}$ while the temperature at 10 mm is $776\text{ }^{\circ}\text{C}$, a difference of $120\text{ }^{\circ}\text{C}$. This temperature difference can in large part be attributed to proximity of the surface layer to the build plate and a lack of thermal buildup after just 33 layers (1.65 mm). However, temperatures can vary between successive layers, as is the case for the peak temperatures at layer heights of 6.25 mm and 6.30 mm, which are $750\text{ }^{\circ}\text{C}$ and $709\text{ }^{\circ}\text{C}$, respectively. This is a temperature difference of $41\text{ }^{\circ}\text{C}$ between annealing steps that are just one layer ($50\text{ }\mu\text{m}$) apart. Given the penetration depth of the surface annealing, such temperature fluctuations will not impede residual stress reduction when annealed well above the critical temperature, but this could be an issue at lower temperatures. Upon close visual observation during printing, there seemed to be a correlation between surface roughness and annealing temperature. Since this annealing process relies on optical absorption of the diode laser energy, the roughness of the top surface plays a significant role. Smoother and more reflective surfaces will have

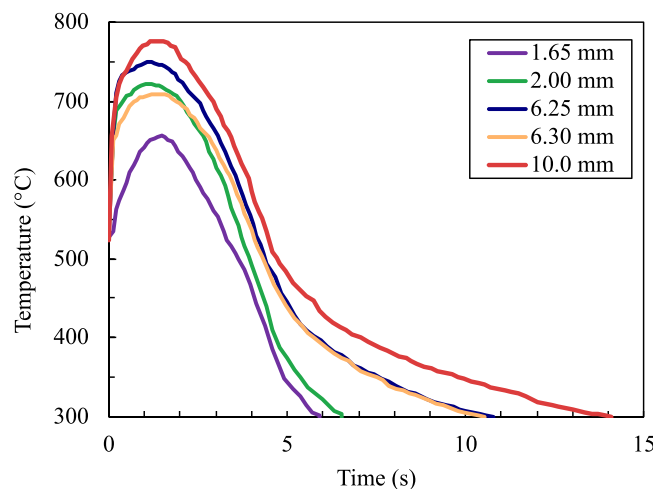


Fig. 9. In situ annealing temperature at the center of the surface as a function of time at select heights.

lower absorption and will consequently reach lower annealing temperatures without increasing the diode laser power. Even when comparing subsequent heated layers, there can be temperature differences above 100 °C within one sample. This fluctuation in annealing temperature may explain some of the differences between the experimental and simulated residual stress results, particularly in the case of the higher temperature samples shown in Fig. 6C and D. Since the mechanical properties of 316L stainless steel change dramatically above 700 °C, a fluctuation in annealing temperature of 100 °C can lead to significant discrepancies [47]. In an effort to find a correlation between roughness and annealing temperature, roughness measurements were made on the top surfaces of the printed samples using a microscope profile scanner (Keyence VR), but no clear correlation emerged. This was in part due to the surface roughness varying from layer to layer, so the roughness of the measurable final layer does not necessarily represent the roughness of all layers within the part.

In addition to the variation in surface roughness, the uniform heat input during the melting stage of the simulations could be a source of discrepancy between experimental and simulated results. This disagreement is particularly true near the top of the samples, as seen in Fig. 6, even for the non-annealed and lower temperature samples. In the simulations, heat was applied uniformly during the melting stage for each layer in order to cut down on simulation time, which is a technique that has been shown to produce reliable residual stress predictions in the past [16,41]. However, the inaccuracies of this uniform heat distribution technique may be more visible in the upper layers where the material experiences fewer thermal cycles.

5. Conclusion

An analysis of the extent of stress reduction obtained using a novel and recently developed in situ annealing process for LPBF was presented through spatial stress distribution maps of multiple planes within 316L stainless steel samples. These results were verified by employing multiple residual stress measurement techniques. These measurement techniques, in conjunction with the numerical simulation, showed that there is a stress reduction of over 90% near the base of the part when annealed every layer and there is an equivalent reduction in residual stress when parts are annealed every five layers, reducing the total annealing time by more than 71%. The results also revealed that in situ annealing could be further explored to determine an optimal surface heating frequency to maintain stress reduction while minimizing processing time. Peak temperatures were hypothesized to be influenced by surface roughness, though the average annealing temperature for a

given diode power level remained consistent. This method of stress reduction has the potential to significantly reduce distortions and improve print reliability of LPBF by building well-annealed parts irrespective of height and could eliminate the need for stress relief post processing.

CRediT authorship contribution statement

William L. Smith: Conceptualization, Methodology, Investigation, Data curation, Writing – original draft, Visualization. **John D. Roehling:** Conceptualization, Methodology, Investigation, Writing – review & editing. **Maria Strantza:** Investigation, Writing – original draft. **Rishi K. Ganeriwala** – Software, Writing – original draft, Formal analysis, Data curation. **Ava S. Ashby** – Software, Formal analysis, Data curation, Writing – review & editing. **Bey Vrancken** – Resources, Writing – review & editing. **Bjørn Clausen** – Investigation, Data curation, Writing – review & editing. **Gabriel M. Guss** – Software, Resources. **Donald W. Brown:** Supervision, Writing – review & editing. **Joseph T. McKeown:** Project administration, Funding acquisition. **Michael R. Hill:** Supervision, Resources, Writing – review & editing. **Manyalibo J. Matthews** – Project administration, Funding acquisition, Conceptualization, Writing – review & editing.

Declaration of Competing Interest

The authors declare the following financial interests/personal relationships which may be considered as potential competing interests: William L. Smith has patent #US16/365029 pending to Lawrence Livermore National Laboratory.

Acknowledgments

This work was performed under the auspices of the United States Department of Energy by Lawrence Livermore National Laboratory (LLNL) under Contract DE-AC52-07NA27344 and by Los Alamos National Laboratory under contract DE-AC52-06NA25396. This work was supported through the LLNL Laboratory Directed Research and Development Program under the project tracking code 18-SI-003, LLNL-JRNL-819863.

References

- [1] W.E. Frazier, Metal additive manufacturing: a review, *J. Mater. Eng. Perform.* 23 (2014) 1917–1928, <https://doi.org/10.1007/s11665-014-0958-z>.
- [2] W.E. King, A.T. Anderson, R.M. Ferencz, N.E. Hodge, C. Kamath, S.A. Khairallah, A.M. Rubenchik, Laser powder bed fusion additive manufacturing of metals: physics, computational, and materials challenges, *Appl. Phys. Rev.* 2 (2015), 041304, <https://doi.org/10.1063/1.4937809>.
- [3] A.A. Martin, N.P. Calta, S.A. Khairallah, J. Wang, P.J. Depond, A.Y. Fong, V. Thamby, G.M. Guss, A.M. Kiss, K.H. Stone, C.J. Tassone, J. Nelson Weker, M.F. Toney, T. van Buuren, M.J. Matthews, Dynamics of pore formation during laser powder bed fusion additive manufacturing, *Nat. Commun.* 10 (2019) 1987, <https://doi.org/10.1038/s41467-019-10009-2>.
- [4] P.A. Hooper, Melt pool temperature and cooling rates in laser powder bed fusion, *Addit. Manuf.* 22 (2018) 548–559, <https://doi.org/10.1016/j.addma.2018.05.032>.
- [5] Ö. Poyraz, M.C. Kuşhan, Residual stress-induced distortions in laser powder bed additive manufacturing of nickel-based superalloys, *SV-JME* 65 (2019) 343–350, <https://doi.org/10.5545/sv-jme.2019.6004>.
- [6] A.S. Wu, D.W. Brown, M. Kumar, G.F. Gallegos, W.E. King, An experimental investigation into additive manufacturing-induced residual stresses in 316L stainless steel, *Met. Mater. Trans. A* 45 (2014) 6260–6270, <https://doi.org/10.1007/s11661-014-2549-x>.
- [7] J.P. Kruth, B. Vandenbroucke, J. Van Vaerenbergh, P. Mercelis, Benchmarking of Different SLS/SLM Processes as Rapid Manufacturing Techniques, 2005. (<https://ris.utwente.nl/ws/portalfiles/portal/5676701/Wa1021.pdf>). (Accessed 24 September 2020).
- [8] J.P. Kruth, L. Froyen, J. Van Vaerenbergh, P. Mercelis, M. Rombouts, B. Lauwers, Selective laser melting of iron-based powder, *J. Mater. Process. Technol.* 149 (2004) 616–622, <https://doi.org/10.1016/j.jmatprotec.2003.11.051>.
- [9] Y. Liu, Y. Yang, D. Wang, A study on the residual stress during selective laser melting (SLM) of metallic powder, *Int. J. Adv. Manuf. Technol.* 87 (2016) 647–656, <https://doi.org/10.1007/s00170-016-8466-y>.

- [10] J.-P. Kruth, J. Deckers, E. Yasa, R. Wauthlé, Assessing and comparing influencing factors of residual stresses in selective laser melting using a novel analysis method, *Proc. Inst. Mech. Eng. Part B: J. Eng. Manuf.* 226 (2012) 980–991, <https://doi.org/10.1177/0954405412437085>.
- [11] P. Mercelis, J.-P. Kruth, Residual stresses in selective laser sintering and selective laser melting, *Rapid Prototyp. J.* (2006) 254–265, <https://doi.org/10.1108/13552540610707013>.
- [12] J.D. Roehling, W.L. Smith, T.T. Roehling, B. Vrancken, G.M. Guss, J.T. McKeown, M.R. Hill, M.J. Matthews, Reducing residual stress by selective large-area diode surface heating during laser powder bed fusion additive manufacturing, *Addit. Manuf.* 28 (2019) 228–235, <https://doi.org/10.1016/j.addma.2019.05.009>.
- [13] P. Aggarangsi, J. Beuth, Localized Preheating Approaches for Reducing Residual Stress in Additive Manufacturing, in: *Proc. SFF Symp.*, Austin, 2006.
- [14] L. Papadakis, D. Chantzis, K. Saloniatis, On the energy efficiency of pre-heating methods in SLM/SLS processes, *Int. J. Adv. Manuf. Technol.* 95 (2018) 1325–1338, <https://doi.org/10.1007/s00170-017-1287-9>.
- [15] L.A. Parry, I.A. Ashcroft, R.D. Wildman, Geometrical effects on residual stress in selective laser melting, *Addit. Manuf.* 25 (2019) 166–175, <https://doi.org/10.1016/j.addma.2018.09.026>.
- [16] M.F. Zaeh, G. Branner, Investigations on residual stresses and deformations in selective laser melting, *Prod. Eng. Res. Dev.* 4 (2010) 35–45, <https://doi.org/10.1007/s11740-009-0192-y>.
- [17] L. Ma, H. Bin, Temperature and stress analysis and simulation in fractal scanning-based laser sintering, *Int. J. Adv. Manuf. Technol.* 34 (2007) 898–903, <https://doi.org/10.1007/s00170-006-0665-5>.
- [18] A. Ulbricht, S.J. Altenburg, M. Sprengel, K. Sommer, G. Mohr, T. Fritsch, T. Mishurova, I. Serrano-Munoz, A. Evans, M. Hofmann, G. Bruno, Separation of the formation mechanisms of residual stresses in LPBF 316L, *Metals* 10 (2020) 1234, <https://doi.org/10.3390/met10091234>.
- [19] M. Strantza, B. Vrancken, M.B. Prime, C.E. Truman, M. Rombouts, D.W. Brown, P. Guillaume, D. Van Hemelrijck, Directional and oscillating residual stress on the mesoscale in additively manufactured Ti-6Al-4V, *Acta Mater.* 168 (2019) 299–308, <https://doi.org/10.1016/j.actamat.2019.01.050>.
- [20] M.B. Prime, Residual stress measurement by successive extension of a slot: the crack compliance method, *Appl. Mech. Rev.* 52 (1999) 75–96, <https://doi.org/10.1115/1.3098926>.
- [21] M.R. Hill, The slitting method, in: *Practical Residual Stress Measurement Methods*, John Wiley & Sons, Ltd, 2013, pp. 89–108, <https://doi.org/10.1002/9781118402832.ch4>.
- [22] P. Pagliaro, M.B. Prime, H. Swenson, B. Zuccarello, Measuring multiple residual-stress components using the contour method and multiple cuts, *Exp. Mech.* 50 (2010) 187–194, <https://doi.org/10.1007/s11340-009-9280-3>.
- [23] B. Vrancken, V. Cain, R. Knutsen, J. Van Humbeeck, Residual stress via the contour method in compact tension specimens produced via selective laser melting, *Scr. Mater.* 87 (2014) 29–32, <https://doi.org/10.1016/j.scriptamat.2014.05.016>.
- [24] M. Salem, S.L. Roux, A. Hor, G. Dour, A new insight on the analysis of residual stresses related distortions in selective laser melting of Ti-6Al-4V using the improved bridge curvature method, *Addit. Manuf.* 36 (2020), 101586, <https://doi.org/10.1016/j.addma.2020.101586>.
- [25] B. Clausen, C.R. D'Elia, M.B. Prime, M.R. Hill, J.E. Bishop, K.L. Johnson, B. H. Jared, K.M. Allen, D.K. Balch, R.A. Roach, D.W. Brown, Complementary measurements of residual stresses before and after base plate removal in an intricate additively-manufactured stainless-steel valve housing, *Addit. Manuf.* 36 (2020), 101555, <https://doi.org/10.1016/j.addma.2020.101555>.
- [26] D.W. Brown, A. Losko, J.S. Carpenter, B. Clausen, J.C. Cooley, V. Livescu, P. Kenesei, J.-S. Park, T.J. Stockman, M. Strantza, In-Situ high-energy x-ray diffraction during a linear deposition of 308 stainless steel via wire arc additive manufacture, *Met. Mater. Trans. A* 51 (2020) 1379–1394, <https://doi.org/10.1007/s11661-019-05605-2>.
- [27] M. Strantza, R.K. Ganeriwala, B. Clausen, T.Q. Phan, L.E. Levine, D. Pagan, W. E. King, N.E. Hodge, D.W. Brown, Coupled experimental and computational study of residual stresses in additively manufactured Ti-6Al-4V components, *Mater. Lett.* 231 (2018) 221–224, <https://doi.org/10.1016/j.matlet.2018.07.141>.
- [28] M.B. Prime, A.T. DeWalld, The contour method, in: *Practical Residual Stress Measurement Methods*, John Wiley & Sons, Ltd, 2013, pp. 109–138, <https://doi.org/10.1002/9781118402832.ch5>.
- [29] M.J. Matthews, G. Guss, D.R. Drachenberg, J.A. Demuth, J.E. Heebner, E.B. Duoss, J.D. Kuntz, C.M. Spadaccini, Diode-based additive manufacturing of metals using an optically-addressable light valve, *Opt. Express* 25 (2017) 11788–11800, <https://doi.org/10.1364/OE.25.011788>.
- [30] A.T. DeWalld, M.R. Hill, Residual Stress in a Thick Steel Weld Determined Using the Contour Method, University of California Davis, 2001 accessed November 27, 2024AD, http://mae.engr.ucdavis.edu/mhill/papers/AD_MRH_thk_weld_cont_v5.pdf.
- [31] M.A.M. Bourke, D.C. Dunand, E. Ustundag, SMARTS – a spectrometer for strain measurement in engineering materials, *Appl. Phys. A* 74 (2002) s1707–s1709, <https://doi.org/10.1007/s003390201747>.
- [32] H.M. Rietveld, A profile refinement method for nuclear and magnetic structures, *J. Appl. Cryst.* 2 (1969) 65–71, <https://doi.org/10.1107/S0021889869006558>.
- [33] B. Clausen, SMARTSware Manual, Los Alamos National Laboratory, 2004. (ftp://ftp.lanl.gov/public/clausen/SMARTSware/SMARTSware_Manual.pdf).
- [34] A.D. Krawitz, R.A. Winholtz, Use of position-dependent stress-free standards for diffraction stress measurements, *Mater. Sci. Eng. A* 185 (1994) 123–130, [https://doi.org/10.1016/0921-5093\(94\)90935-0](https://doi.org/10.1016/0921-5093(94)90935-0).
- [35] M.R. Daymond, The determination of a continuum mechanics equivalent elastic strain from the analysis of multiple diffraction peaks, *J. Appl. Phys.* 96 (2004) 4263–4272, <https://doi.org/10.1063/1.1794896>.
- [36] C.W. Properties of Stainless Steel AISI Type 316L, 2020. (https://www.efunda.com/materials/alloys/stainless_steels/show_stainless.cfm?ID=AISI_Type_316L&show_prop=all&Page_Title=AISI%20Type%20316L). (Accessed 18 November 2020).
- [37] N.E. Hodge, R.M. Ferencz, J.M. Solberg, Implementation of a thermomechanical model for the simulation of selective laser melting, *Comput. Mech.* 54 (2014) 33–51, <https://doi.org/10.1007/s00466-014-1024-2>.
- [38] J.M. Solberg, N.E. Hodge, M.A. Puso, S.T. Castonguay, R.K. Ganeriwala, R. M. Ferencz, Diablo, A Parallel, Implicit Multi-physics Finite Element Code for Engineering Analysis User Manual, Lawrence Livermore National Laboratory, 2018.
- [39] L. Demkowicz, Ph Devloo, J.T. Oden, On an h-type mesh-refinement strategy based on minimization of interpolation errors, *Comput. Methods Appl. Mech. Eng.* 53 (1985) 67–89, [https://doi.org/10.1016/0045-7825\(85\)90076-3](https://doi.org/10.1016/0045-7825(85)90076-3).
- [40] R.K. Ganeriwala, N.E. Hodge, J.M. Solberg, Towards improved speed and accuracy of laser powder bed fusion simulations via multiscale spatial representations, *Comput. Mater. Sci.* 187 (2021), 110112, <https://doi.org/10.1016/j.commatsci.2020.110112>.
- [41] R.K. Ganeriwala, M. Strantza, W.E. King, B. Clausen, T.Q. Phan, L.E. Levine, D. W. Brown, N.E. Hodge, Evaluation of a thermomechanical model for prediction of residual stress during laser powder bed fusion of Ti-6Al-4V, *Addit. Manuf.* 27 (2019) 489–502, <https://doi.org/10.1016/j.addma.2019.03.034>.
- [42] J. Trapp, A.M. Rubenichik, G. Guss, M.J. Matthews, In situ absorptivity measurements of metallic powders during laser powder-bed fusion additive manufacturing, *Appl. Mater. Today* 9 (2017) 341–349, <https://doi.org/10.1016/j.apmt.2017.08.006>.
- [43] M.D. Olson, A.T. DeWalld, M.R. Hill, Validation of a contour method single-measurement uncertainty estimator, *Exp. Mech.* 58 (2018) 767–781, <https://doi.org/10.1007/s11340-018-0385-4>.
- [44] M.D. Olson, A.T. DeWalld, M.B. Prime, M.R. Hill, Estimation of uncertainty for contour method residual stress measurements, *Exp. Mech.* 55 (2015) 577–585, <https://doi.org/10.1007/s11340-014-9971-2>.
- [45] Stress-relief heat treating of steel[1], in: J.L. Dosssett, G.E. Totten (Eds.), *Steel Heat Treating Fundamentals and Processes*, ASM International, 2013, pp. 275–279, <https://doi.org/10.31399/asm.hb.v04a.a0005782>.
- [46] N.A. Stainless, Long Products Stainless Steel Grade Sheet, 2010. (<https://www.northamericanstainless.com/wp-content/uploads/2010/10/Grade-316-316L1.pdf>).
- [47] American Iron and Steel Institute (last), High-Temperature Characteristics of Stainless Steels, Nickel Development Institute, 2020. (https://nickelinstitute.org/media/4657/nl_aisi_9004_hightemperaturecharacteristics.pdf).
- [48] A. Zafari, M.R. Barati, K. Xia, Controlling martensitic decomposition during selective laser melting to achieve best ductility in high strength Ti-6Al-4V, *Mater. Sci. Eng. A* 744 (2019) 445–455, <https://doi.org/10.1016/j.msea.2018.12.047>.
- [49] W. Xu, M. Brandt, S. Sun, J. Elambasseri, Q. Liu, K. Latham, K. Xia, M. Qian, Additive manufacturing of strong and ductile Ti-6Al-4V by selective laser melting via in situ martensite decomposition, *Acta Mater.* 85 (2015) 74–84, <https://doi.org/10.1016/j.actamat.2014.11.028>.